Synthetic molecular motor activates drug delivery from polymersomes

Guinart, Ainoa; Korpidou, Maria; Doellerer, Daniel; Pacella, Gianni; Stuart, Marc C A; Dinu, Ionel Adrian; Portale, Giuseppe; Palivan, Cornelia; Feringa, Ben L

Published in:
Proceedings of the National Academy of Sciences of the United States of America

DOI:
10.1073/pnas.2301279120

Publication date:
2023

PNAS RESEARCH ARTICLE | CHEMISTRY
APPLIED BIOLOGICAL SCIENCES

Synthetic molecular motor activates drug delivery from polymersomes

Ainoa Guinart[a], Maria Korpidou[b], Daniel Doellerer[a], Gianni Pacella[c], Marc C. A. Stuart[a], Ionel Adrian Dinu[b,d], Giuseppe Portale[c], Cornelia Palivan[b,d,e,1], and Ben L. Feringa[a,c,1]

Edited by Richard Zare, Stanford University, Stanford, CA; received January 27, 2023; accepted April 27, 2023

The design of stimuli-responsive systems in nanomedicine arises from the challenges associated with the unsolved needs of current molecular drug delivery. Here, we present a delivery system with high spatiotemporal control and tunable release profiles. The design is based on the combination of an hydrophobic synthetic molecular rotary motor and a PDMS-*b*-PMOXA diblock copolymer to create a responsive self-assembled system. The successful incorporation and selective activation by low-power visible light (λ = 430 nm, 6.9 mW) allowed to trigger the delivery of a fluorescent dye with high efficiencies (up to 75%). Moreover, we proved the ability to turn on and off the responsive behavior on demand over sequential cycles. Low concentrations of photoresponsive units (down to 1 mol% of molecular motor) are shown to effectively promote release. Our system was also tested under relevant physiological conditions using a lung cancer cell line and the encapsulation of an Food and Drug Administration (FDA)-approved drug. Similar levels of cell viability are observed compared to the free given drug showing the potential of our platform to deliver functional drugs on request with high efficiency. This work provides an important step for the application of synthetic molecular machines in the next generation of smart delivery systems.

molecular motor | polymersome | drug delivery | light-responsive | cancer

Significance

Our work presents the incorporation of synthetic rotary molecular motors into a block copolymer assembly to enable controlled drug release. We overcome one of the major drawbacks of photoresponsive molecules by using low-power visible light for the activation. Only low quantities (1 mol%) of molecular motor are needed for efficient release which facilitates scale-up and clinical translation. We prove its nontoxicity under physiological conditions and reach similar levels of action when compared to the free-administrated approved antitumor drug in a lung carcinoma cell line. Our system offers advantages to the free-drug approach as the encapsulation protects the drug against environmental adverse effects. These results represent an unprecedented approach in the field of smart drug delivery.

Nanomedicine, defined as the engineering of functional systems at the molecular level for medical applications, has seen rapid progress during the past decades (1–4). While its applications are broad, and new opportunities are rapidly evolving, one of the most established and relevant fields of nanomedicine is its implementation in drug delivery systems (5, 6). These platforms allow one to transport otherwise toxic chemicals into or throughout the body, to exploit multiple mechanisms of action by changing the uptake route of the drugs, and to maximize efficiencies by increasing bioavailability alongside with reducing dosages (7–9). Since the discovery of the liposome structure in 1964 (10), drug delivery systems have strongly evolved as a prominent field of science (11–13). In 1995, the first nanotherapeutic was approved by the FDA starting clinical validation and commercialization of the field (14, 15).

Although lipid-based nanosystems are cost-effective and show good drug entrapment efficiencies, they often suffer from low stabilities, high polydispersity indexes (PDIs), and limited possibilities for surface modifications (16–18). These limitations are overcomed by polymer-based nanosystems as they show higher stabilities, tunability, robustness, cargo retention, life-span, and modular chemistries (12, 19–21). Based on these features, the use of polymeric nanomaterials in the development of new medicines is now recognized by the European Union as a key enabling technology to address unmet medical needs (22).

In recent years, stimuli-responsive delivery systems have appeared as a promising approach to better control the administration of drugs (2, 23–25). These systems undergo a physical or chemical transformation in response to an external stimulus to trigger precise delivery of the medicine. Various triggers can be used to promote release from these systems such as a change in pH (26), temperature (27), magnetic field (28), ultrasound (29), electrical stimulation (30) or enzymes (31), among others, as summarized in this extensive review (32). Amidst all these stimuli, light is the one that can be better focused and regulated, allowing for higher temporal and spatial control together with a deep penetration and a low toxicity in the human body (provided that visible or infrared wavelengths are used) (33).

On the other hand, photoswitches have been widely utilized in light-actuated drug delivery due to their ability to undergo conformational changes upon irradiation (34). Among them, azobenzenes are the most widely employed, although other photoresponsive molecules such as spiropyrans have been reported (35, 36). However, so far, light-responsive delivery systems have not made it into clinical trials, and most of them still suffer from

Author contributions: A.G., M.K., C.P., and B.L.F. designed research; A.G., M.K., D.D., G. Pacella, and M.C.A.S. performed research; A.G., M.C.A.S., I.A.D., and G. Portale analyzed data; C.P. and B.L.F. supervised the research; C.P. and B.L.F. acquired funding; and A.G. and M.K. wrote the paper.

The authors declare no competing interest.

This article is a PNAS Direct Submission.

[1]To whom correspondence may be addressed. Email: cornelia.palivan@unibas.ch or b.l.feringa@rug.nl.

This article contains supporting information online at https://www.pnas.org/lookup/suppl/doi:10.1073/pnas.2301279120/-/DCSupplemental.

Published June 26, 2023.

severe limitations (37). To summarize some of the challenges, most strategies only function under UV light, which suffers from limited penetration and high ionizing toxicity within the body (38, 39). Other disadvantages include poor control over the release process , as many systems operate in an open-loop fashion, releasing all its content in response to the stimuli which fails improving the delivery of highly toxic drugs (40). An additional problem is the high concentrations of photoresponsive molecules required to operate the systems, making them expensive and lowering their value for medical translation. Furthermore, a limited number of photoisomerizable molecules are available and there are still many concerns about their biocompatibility (41). For instance, in the case of azobenzene, an enzyme produced by bacteria in the gastrointestinal tract, azoreductase, can degrade the molecule into products such as nitrobenzene considered toxic by the FDA (42–44).

Emerging from chiroptical molecular switches, a more controlled motion can be achieved by the so-called light-driven synthetic molecular motors (45). These molecules fulfill three basic requirements of a motorized machine: a complete 360 ° unidirectional rotation, repetitive motion, and energy consumption. Extensive reviews about the design of light-driven rotary molecular motors have been published (45, 46). Overcrowded alkene motors were presented by our group in 1999, becoming the first molecules able to undergo photochemically powered unidirectional rotation across a double bond (47). In recent years, the field has rapidly progressed and developed, making it possible to adapt the molecular design to a broad range of applications, including actuators, mechanically dynamic responsive materials, surfaces, and artificial muscles (48–51).

Our approach here is to incorporate a light-driven molecular motor into a $PDMS_{25}$-*b*-$PMOXA_{10}$ diblock copolymer delivery system (Fig. 1). We envision to obtain a higher degree of control and enhanced delivery efficiencies by making use of the continuous rotation of molecular motors. In contrast to switches, we anticipate progressively driving the multicomponent system out of equilibrium by generating effective mechanical work. A more efficient system is expected to allow for lower quantities of responsive material, thereby reducing the cost and toxicity of the delivery system without compromising its responsive behavior. Hence, the use of a single wavelength of visible light facilitates its use in medical setups (e.g. by clinical lasers). In the present study, we report on the synthesis and physicochemical characterization of a visible-light responsive polymersome based on a rotary molecular motor, along with its morphological changes under irradiation

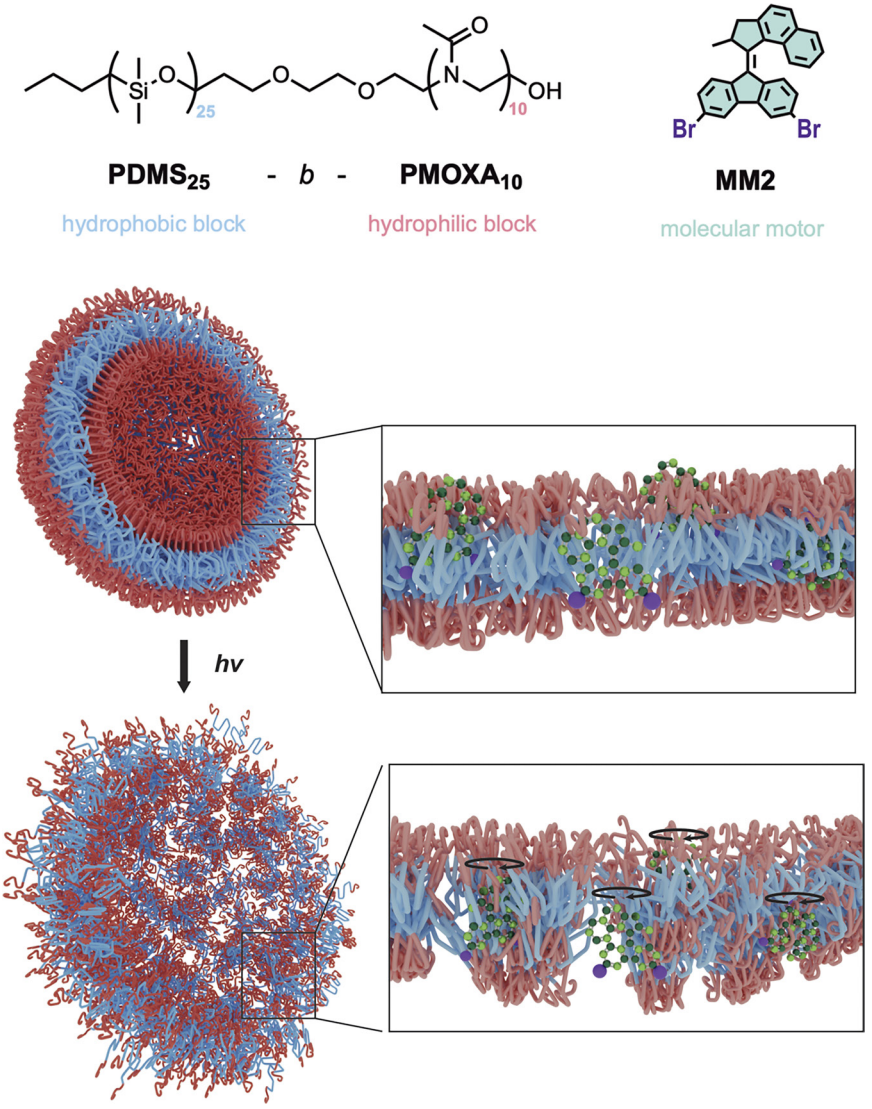

Fig. 1. Chemical structure of the $PDMS_{25}$-*b*-$PMOXA_{10}$ diblock copolymer and molecular motor MM2 (*Top*). Schematic representation of the vesicular system and magnification region of the multicomponent motor-block copolymer assembly in the bilayer of the delivery system (*Bottom*). (MM2 not to scale).

and cargo release when loaded with a fluorescent dye. Furthermore, we explore the potential of our approach for therapeutic applications. Specifically, we evaluate the delivery and cellular effects of our system in a lung carcinoma-derived model when encapsulating the hydrophilic drug pemetrexed (PEM) in our polymersomes.

1. Results

1.1. Synthesis and Characterization of Molecular Motor—Diblock Copolymer System. Amphiphilic diblock copolymer $PDMS_{25}$-*b*-$PMOXA_{10}$ consisting of hydrophobic poly(dimethylsiloxane) (PDMS) and hydrophilic poly(2-methyl-2-oxazoline) (PMOXA) blocks was synthesized via sequential ionic polymerization according to a procedure reported previously (52). This polymer has already shown to be promising for several biological applications due to its low toxicity, stability, and protective effect on enzymes against protease degradation (53–55). In this study, we envisioned to incorporate a synthetic, light-responsive, dibromomolecular motor (**MM2**) into the hydrophobic domain of the block copolymer membrane, aiming to achieve precise control of the opening of the polymersomes (Fig. 1).

MM2, the light-responsive motor, was synthesized as detailed in *SI Appendix*, modifying our earlier reported procedure (56). The improved synthesis allows for scale-up productionwith fewer steps and cheaper materials. In addition to its translational value, this molecular motor also features a small size (~1 nm length and molecular weight of 502 g mol^{-1}) and a high hydrophobicity, which ensures its successful incorporation into the polymersome membrane. The choice of two bromine atoms in the structure aligns with the growing interest in medicinal chemistry to include bulky halogen elements, as they contribute to the destabilization of supramolecular complexes through steric effects and intramolecular interactions (57). Furthermore, the wavelength of activation of **MM2** falls into the visible range (λ=420 or 430 nm were used in this study) which makes it suitable for biological applications. Additionally, this molecular motor operates at a rapid rotational speed (half-life of 0.3 s at 37 °C), which has been proved to be crucial when disrupting amphiphilic systems (58).

A self-assembly of the motor-embedded polymersomes was achieved by means of thin film hydration to obtain vesicles of ~150 nm diameter and a ~9 nm bilayer membrane thickness. Representative cryogenic transmission electron microscopy (cryo-TEM) micrographs of an empty polymersome (EP) and one containing 25 mol% of **MM2** are shown in Fig. 2 *A* and *B*, respectively. Additional morphological characterizations are shown in *SI Appendix*, Fig. S1 and Table S1. Different vesicular systems were studied varying the concentration (in mol%) of **MM2** in the hydrophobic domain of the membrane.

Incorporation of **MM2** inside the polymer bilayer was also evaluated using small-angle X-ray diffraction (SAXS). Intensity profiles for the $PDMS_{25}$-*b*-$PMOXA_{10}$ EPs and the polymersome loaded with **MM2** (Ps_**MM2**) are shown in Fig. 2*C*. Intensity oscillations in the q-range 0.2 to 2 nm^{-1} are related to the thickness and the electron density profile of the polymersome membrane. Generally, it can be observed that the position of the oscillations does not shift upon motor incorporation, suggesting that the membrane thickness does not change between the two samples. Remarkably, the amplitude of the oscillation does change, indicating change of the difference between the electron density of the inner and the outer part of the bilayer membrane.

The SAXS profiles were fitted using a model for a spherical polymersome with a bilayer membrane with Gaussian electron density profiles (59). Since the size of the polymersome is outside of the measured q-range, it was kept fixed to 200 nm in agreement

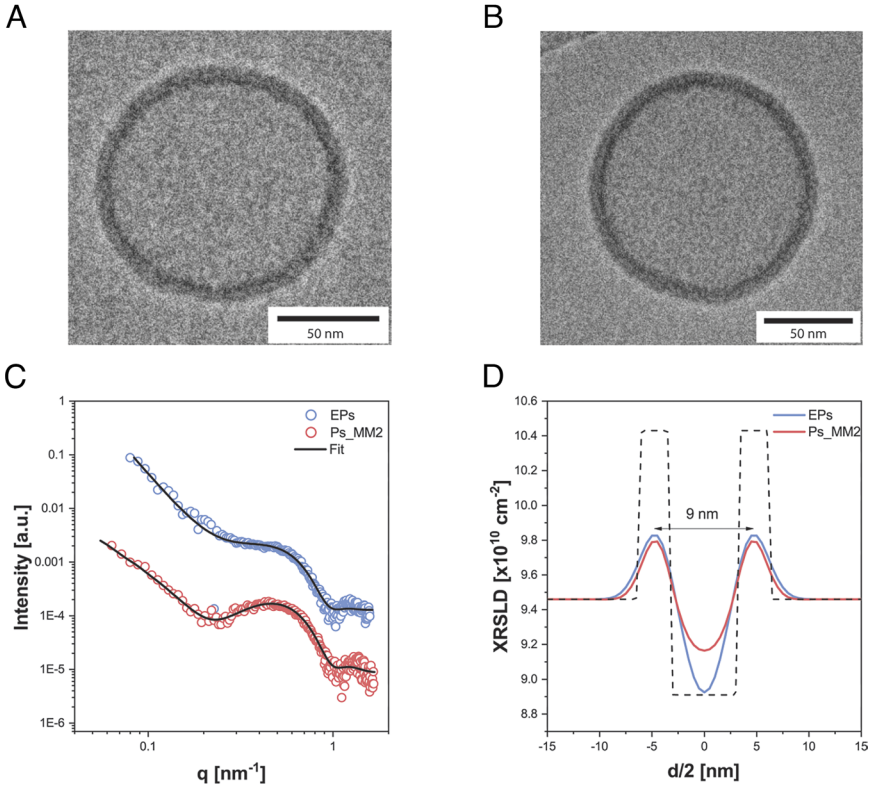

Fig. 2. Morphological characterization of polymersomes. (*A*) cryoTEM image of empty $PDMS_{25}$-*b*-$PMOXA_{10}$ polymersome. (*B*) cryoTEM image of $PDMS_{25}$-*b*-$PMOXA_{10}$ polymersome containing 25 mol% MM2. (*C*) SAXS intensity profiles for EPs and Ps_MM2 systems, along with the fitted curves. (*D*) Extracted X-ray scattering density profiles. The dashed line represents the expected values for the bulk PMOXA and PDMS layers. The 0 value is placed in the center of the inner polymersome layer.

with the transmission electron microscopy (TEM) observations. The calculated X-ray scattering length density profiles are shown in Fig. 2*D*. In agreement with the molecular structure, the PDMS layer shows a lower scattering length density with respect to water, while the PMOXA layers have higher scattering length density (60). As expected, the PMOXA layers are substantially swollen by water, showing a scattering length density sensibly lower than the expected bulk value. The distance between the centers of the PMOXA outer layers is calculated to be 9 nm, in close agreement with the wall thickness observed by TEM. The system with **MM2** shows a clear increase of the electron density of the inner membrane layer, clearly confirming the successful incorporation of the motor in the hydrophobic PDMS layer.

Dynamic light scattering (DLS) was used to verify the presence of vesicles and to obtain information about their hydrodynamic diameter (D_h) and size distribution (reported as; PDI). Static light scattering (SLS) revealed the radius of gyration (R_g) and the DLS profile the hydrodynamic radius (R_h). The R_g/R_h or shape parameter ρ was around 1, which corresponds to spheres (*SI Appendix*, Fig. S2) (61). By measuring their z-potential, a slight increase in their net charge was observed with increasing molecular ratios of **MM2**, indicating its incorporation (*SI Appendix*, Table S2) (62). Their colloidal stability was also confirmed, as no aggregation was observed during the characterization process. The physicochemical characteristics of MM2, a highly aromatic conjugated uncharged system, makes it a strong lipophilic molecule. Its solubility in water is very low, and if the molecule happened to be washed out of the polymer system, it would aggregate or sediment in the media. Notice that such aggregates would be visible during *cryo*-TEM analysis. To point out this phenomena, a range of MM2 aggregates within the concentrations studied in the manuscript were evaluated under dynamic light scattering and their profiles included in *SI Appendix*, Fig. S3 and Table S3. Number fluctuations or multiple scattering of the samples were discarded after ensuring a good quality of the data with a correlation intercept close to 1. The insertion of MM2 did not affect the size of the polymersomes significantly, and was successful in all molecular ratios studied (0.5 to 50 mol%, *SI Appendix*, Figs. S4–S11) with a mean encapsulation efficiency (%) of 74.57 ± 18, assessed by UV spectroscopy after purification of the samples by size exclusion chromatography (SEC) (*SI Appendix*, Table S4). The saturation content of MM2 was found to be 25 mol% (*SI Appendix*, Fig. S12). A plateau phase is reached after increasing the concentration of **MM2** if the absorbance value at 400 nm is followed. The maximum absorbance of **MM2** is located at this value and is directly proportional to **MM2** content (63). The structural and functional stability of $PDMS_{25}$-*b*-$PMOXA_{10}$ polymersome systems has been deeply studied in physiological conditions for up to 6 months (64). As combination of the system with **MM2** had not been done before, and we carried out stability studies accordingly. Samples were found to be structurally stable for over a week (*SI Appendix*, Fig. S13) and up to 6 months when stored at 4 °C in the dark (*SI Appendix*, Fig. S14).

1.2. Morphological Changes Under Visible Light Irradiation. Overcrowded alkene molecular motors are able to undergo unidirectional rotation across the central double bond (rotary axle) when irradiated with light. The 360° rotation cycle is possible as the molecule undergoes four sequential steps in an overall unidirectional manner (46). The process is characterized by two photochemical *E-Z* isomerizations each followed by a thermal helix inversion step that brings the system back to the initial state after a full unidirectional rotation, resulting in continuous motion as long as there is a photon supply. In short, continuous motion persists as long as the sample is exposed to light of the appropiate wavelength (46).

Fig. 3 and *SI Appendix*, Figs. S4–S11 shows how the absorption spectra of the polymersome samples changes under irradiation with visible light. A characteristic exponential decay (200 to 250 nm) indicates the presence of diblock copolymer vesicles and the spectral change of the **MM2** absorption peak (λ_{max} = 405 nm) corresponds to the successful photochemical *E-Z* isomerization and thus the rotation of the molecular motor inside the polymersomes.

The influence of visible light irradiation on the morphology of polymersomes was also evaluated. DLS measurements on control vesicles irradiated for 1 min with 420 nm light did not show a significant change in their D_h of 100 or 200 nm (Fig. 4*A* and *SI Appendix*, Fig. S5). However, in the case of polymersomes

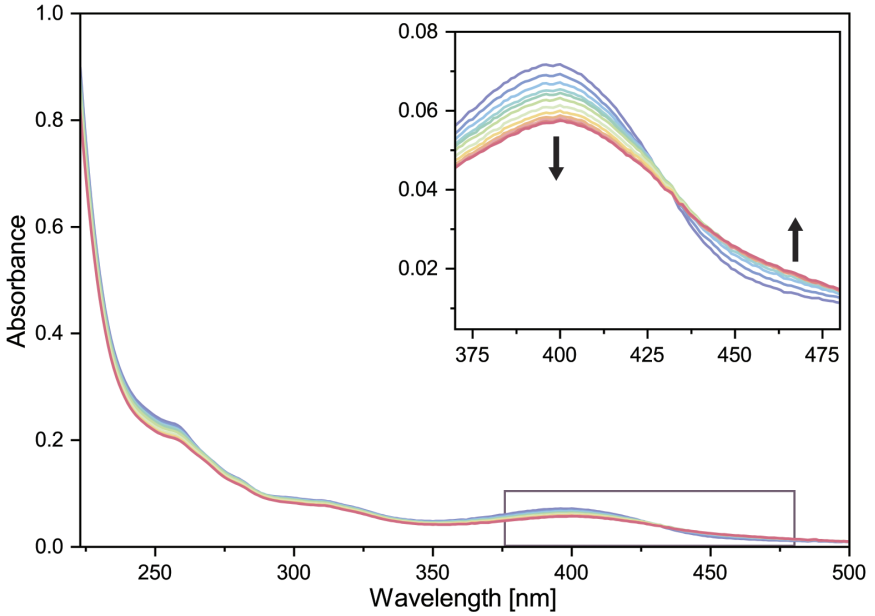

Fig. 3. Visible light (30 s, λ = 420 nm, 6.9 mW) irradiation of aqueous solution of polymersome with 10 mol% MM2. *Inset* showing the MM2 absorption peak changes due to light irradiation and the isosbestic point, as indication of selective *E-Z* isomerization across the double bond.

containing 25 mol% of **MM2**, measurements on the sample concentration using nanoparticle tracking analysis (NTA) did show a significant decrease in the amount of vesicles present, indicating a disruption of particles (Fig. 4 *B* and *C*). We also observed a change in the homogeneity of size distribution by means of volume denoting a population alteration after sample irradiation (Fig. 4*D*). Changes in the PDI and correlation function intercept of irradiated vesicles were not significant and can be found in *SI Appendix*, Table S4.

To further study the effect of irradiation on the shape and structure of the vesicles we analyzed them using TEM and cryo-TEM. Micrographs before irradiation showed the usual shape of spherical polymersomes (Fig. 5*A*). After irradiating for 1 min with visible light (λ = 420 nm, 6.9 mW), an obvious change was observed in all samples containing **MM2**. Clear bursting of the vesicles is shown in Fig. 5*B* and the loss of the three-dimensional structure after irradiation can be noticed. The wrinkled oval-shaped appearance is representative of a three-dimensional nature after negative staining, indicating a hollow sphere structure which disappears after irradiation (Fig. 5*C*). These results are a visible indication of the ability of MM2 to open polymer vesicles using exclusively light energy as fuel.

1.3. On/Off Release Behavior of a Fluorescent Dye. We next investigated the release profile from our polymersomes and how it could be controlled on-demand using light. Here, calcein was employied as a fluorescent probe as its release is often used in vesicular systems due to its self-quenching fluorescence behavior (65). Polymersomes loaded with a calcein concentration above the self-quenching value exhibit tnonfluorescent values. Only when release occurs from the vesicles, the concentration drops, mixing with the calcein-free environment, and fluorescence starts to increase (Fig. 6*A*). By measuring the fluorescence intensity before and after sequential irradiations and comparing it to complete release (by disrupting the systems by adding 1% EtOH under sonication for 15 min), the release percentage can be determined over time. All polymersomes (with/without **MM2**) were loaded with 20 mM calcein solution in phosphate buffered saline (PBS) with an average encapsulation efficiency of 67 ± 2%, still in the self-quenched regime (*SI Appendix*, Table S5). Samples were subjected to the same irradiation setup; an initial fluorescence measurement was taken before any light exposure. Then, all polymersome solutions were irradiated for 1 min with visible light (λ = 420 nm, 6.9 mW) and another measurement was performed. Subsequently, polymersome solutions were kept in the dark for 30 min to evaluate release kinetics and a final measurement was taken before irradiating again. This process was repeated during three irradiation cycles (Fig. 6*B*).

Fig. 6*C* illustrates the release profile of polymersomes containing 0, 1, 5, or 25 mol% of **MM2**. Calcein-loaded polymersomes without **MM2** present did not show a significant release at any time point during the sequential irradiations, as expected, **MM2**

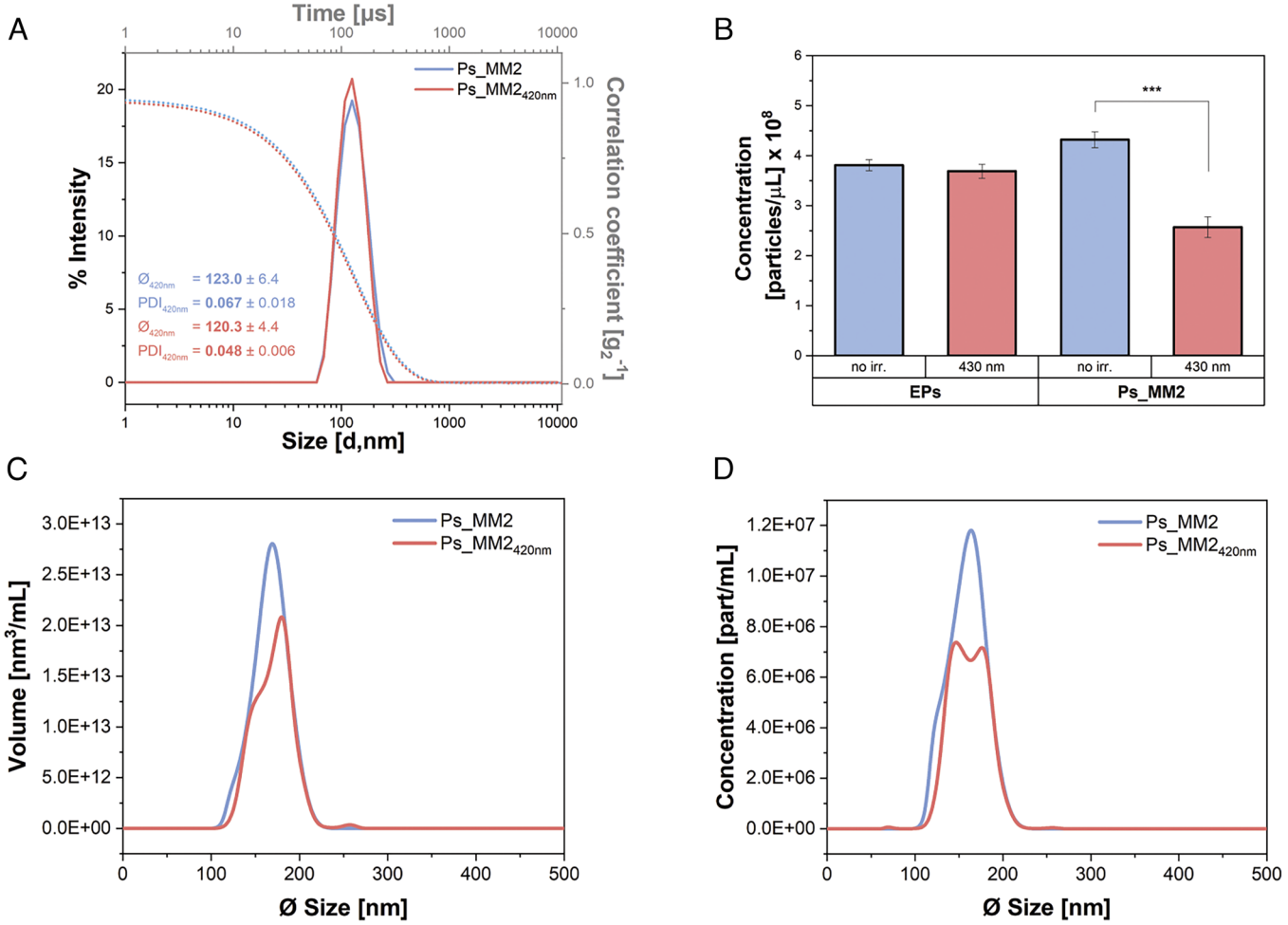

Fig. 4. Morphological changes under visible light irradiation. (*A*) DLS intensity size distribution and correlation function of non/irradiated vesicles. (*B*) NTA concentration size distribution of non/irradiated vesicles. (*C*) NTA volume size distribution of non/irradiated vesicles. (*D*) Change in the concentration of EPs and Ps_MM2 after irradiation distribution analyzed by NTA. All samples containing MM2 at a concentration of 25 mol%. All irradiations were performed under the same irradiation conditions (1 min, λ = 420 nm, 6.9 mW). ***indicates statistically significant data ($P \leq 0.001$).

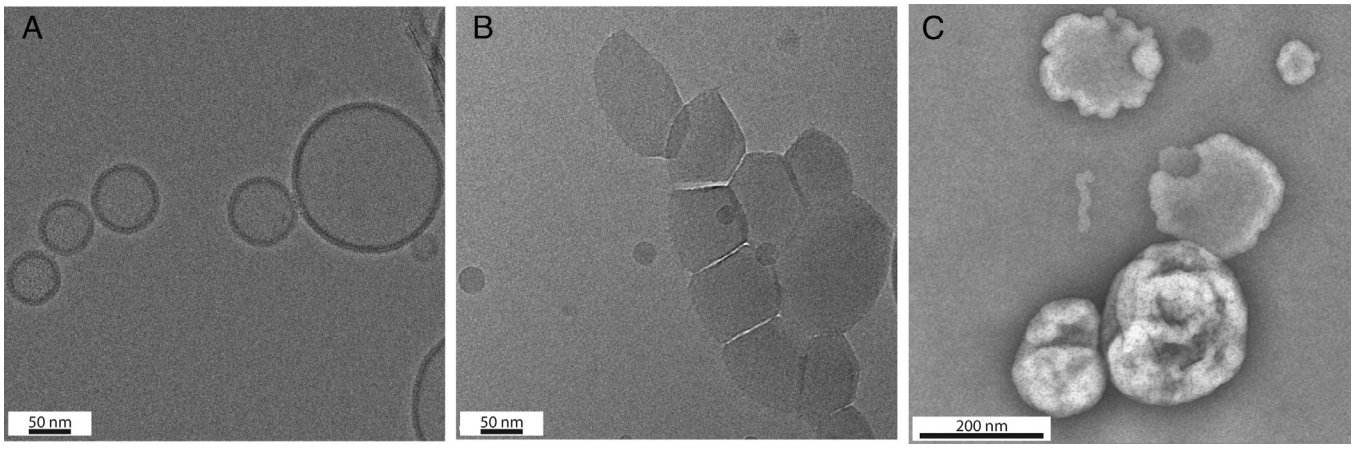

Fig. 5. Transmission electron microscopy images of polymersomes containing 25 mol% MM2. (*A*) cryoTEM image before irradiation. (*B*) cryoTEM image after irradiation. (*C*) TEM image after irradiation showing two bursted (*Top*) and two entire polymersomes (*Bottom*). Irradiations done λ = 420 nm, 1 min and 6.9 mW.

being the light-responsive unit. For calcein-loaded polymersomes containing 1, 5 and 25 mol% of MM2 the first irradiation event triggered the largest release content, up to 21, 24, and 52%, respectively. Subsequent irradiations were able to increase the release by ~18% each. Most interestingly, release was completely suppressed when stopping the light input showing that no vesicles were bursting without irradiation. A small decrease in the release can be observed when keeping the samples in the dark for 30 min after irradiation which we attribute to small bleaching of the released dye. Fig. 6*D* shows the percentage of calcein release after the first and last irradiation for the different **MM2** concentrations. Release was increased by 37%, 29%, and 42% with 1, 5, and 25 mol% of **MM2**, respectively, between the first and third cycle. Total release after three irradiations was found to be highly effective for 25 mol% **MM2** samples (around 75%). Notibly, even with low concentration of the molecular motor, such as 1 mol% **MM2**, a significant release of around 30% was observed . A sustained release over time was also achieved by constant irradiation of polymersomes with 25 mol% of **MM2** (*SI Appendix*, Fig. S15) demonstrating a control on the release behavior by manipulating

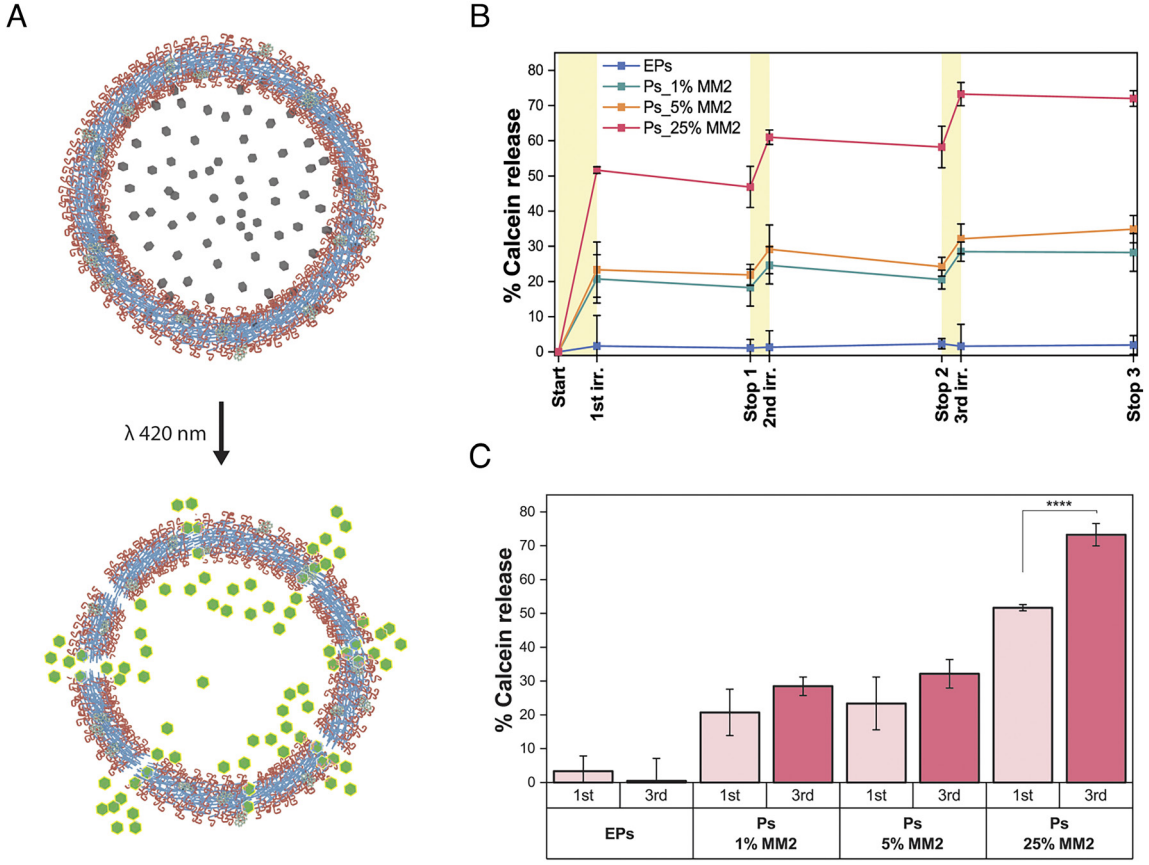

Fig. 6. Calcein release studies. (*A*) Self-quenching behavior of calcein dye and induced light-release from polymersome vesicles. (*B*) Percentage of calcein release during sequential irradiations over different concentrations of MM2. Yellow bars indicate the period when samples are under irradiation conditions. Data points show the mean ± SD of three independent experiments. (*C*) Percentage of calcein release after the first irradiation (light) and the third (dark) for each of the different conditions. **** indicates statistical significance with P <0.0001.

the irradiation conditions. These results establish not only a competent release for small guest molecules encapsulated in the vesicles with very small amounts of light-responsive motor, but also a precise temporal control on the release behavior being able to switch the system on and off on demand.

1.4. PEM Delivery in Cells. Next, we investigated the potential of Ps_**MM2** to function as a drug delivery system in cells. PEM is a drug approved for the treatment of pleural mesothelioma and nonsmall cell lung cancer (66). However, due to its high hydrophilicity and polarity, strategies to increase its permeability and bioavailability have been developed (67–69). In our approach for a light-controlled delivery system, PEM was encapsulated in the aqueous cavity of polymersomes equipped with the synthetic molecular motor (Ps_**MM2**_PEM). The drug encapsulation efficiency was calculated at 43 ± 7% based on SEC (*SI Appendix*, Fig. S16). Subsequently, we explored the effects of irradiation on cells with or without drug treatment. Adenocarcinomic human alveolar basal epithelial cells (A549) were incubated with PEM (5 μM) or the respective amount of PBS and were irradiated at 430 nm for 1 min. In the conducted experiment it was shown that the irradiation by itself had no effect on cell viability (Fig. 7*A* and *SI Appendix*, Fig. S17) As expected, exposure of nonirradiated A459 cells to PEM reduced cell viability to about 60% ($P < 0.00001$).

However, no further reduction was observed when PEM-treated cells were irradiated, even after 24 h of incubation ($P = 0.00042$) (Fig. 7*A*). To evaluate the drug release from Ps_**MM2**_PEMs and its efficacy, Ps_**MM2**_PEMs that were irradiated at 430 nm for 1 min were centrifuged to remove ruptured membranes, and the supernatant was used for the incubation with cells. Based on the encapsulation efficiency and the calcein release studies, we calculated the final PEM concentration to match the free-drug-treated cells at 5 μM. Consistent with this observation, the viability of cells treated with Ps_**MM2**_PEM supernatant was also reduced to 60% ($P < 0.000001$) (Fig. 7*A*).

After establishing the effects of irradiation and PEM on cell viability, we incubated A549 cells with intact polymersomes for 24 h. Polymersomes with PDMS as the hydrophobic domain and PMOXA the hydrophilic one have been previously shown to be internalized by cells and preserve their integrity for up to 48 h (55, 70). The next day, extracellular polymersomes were removed by washing and cells irradiated at 430 nm for at least 1 min. After a subsequent 24 h incubation, the cell viability was assessed (Fig. 7*B*). Compared to irradiated cells lacking polymersomes, cells containing Ps_**MM2**_PEM showed a decrease in cell viability to 60% in response to irradiation, as was observed for cells treated with free PEM ($P = 0.00029$). In the case of cells incubated with Eps, Ps_**MM2,** and Ps_PEM, cell viability was not significantly decreased, irrespective of irradiation. Taken together, these findings indicate that neither the polymer (EPs) nor the synthetic molecular motor entrapped in the hydrophobic domain of the polymer membrane (Ps_**MM2**) are cytotoxic at the concentrations used for polymersome assembly (55). The structural integrity of polymersomes within cells is evidenced by the lack of decrease in cell viability in the case of PSs_PEM and PSs_MM2_PEM nonirradiated. More importantly, cytotoxicity of Ps_**MM2**_PEMs is dependent on irradiation, inducing a conformational change of membrane-embedded synthetic molecular motors, which in turn causes the membrane to disrupt and release PEM. Based on

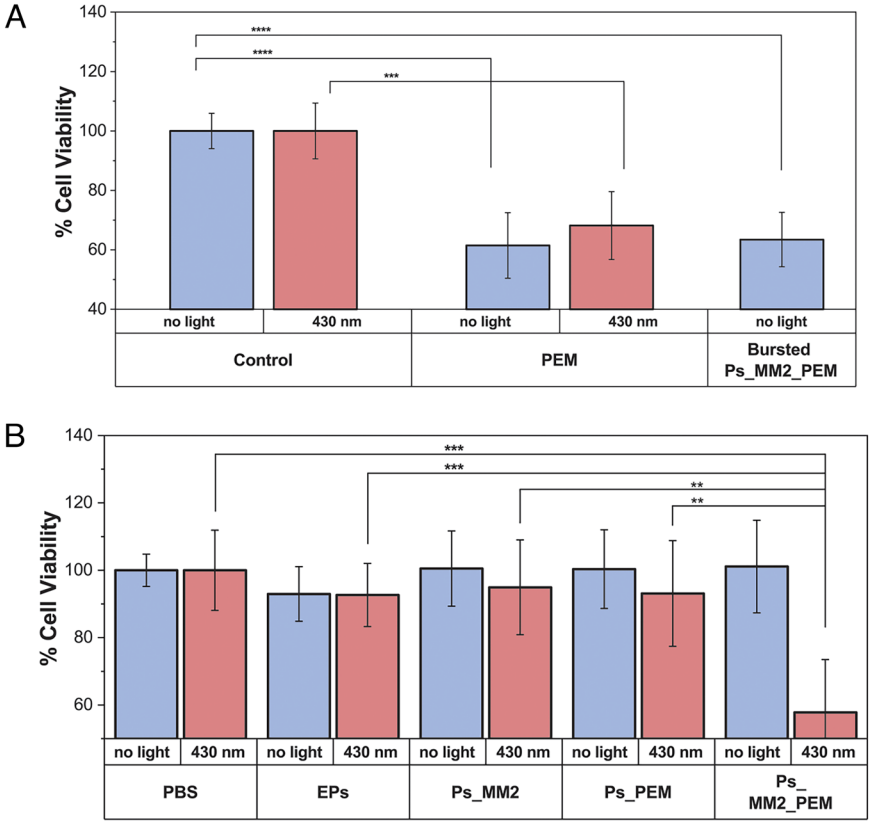

Fig. 7. (*A*) Cell viability as percentage of irradiated (λ = 430 nm, 1 min) and nonirradiated A549 cells incubated with only PBS (control), 5 μM PEM and supernatant of irradiated Ps_MM2_PEM (5 μM PEM) (*B*) Cell viability as percentage of irradiated (λ = 430 nm, 1 min) and nonirradiated A549 cells incubated with only PBS (control), EPs, Ps_MM2, Ps_PEM and Ps_MM2_PEM. Graph shows mean ± SD of three independent experiments. Statistically significant data (****, ***, ** equivalent to a $P \leq 0.0001$, ≤ 0.001 and ≤ 0.01, respectively).

previous studies and the mechanism of action of PEM, we consider that the polymersomes internalized by cells preserve their integrity in the cytoplasm where they release their hydrophilic cargo upon irradiation (70, 71). These experiments with A549 carcinoma cell line and the molecular motor-based vesicles Ps_**MM2**_PEM show that the presence of molecular motor and light irradiation are necessary to promote drug release.

2. Discussion

In the present study, we demonstrate for the first time the use of synthetic molecular motors in a stimuli-responsive polymer-based drug delivery system. In our case, the unidirectionality and continuous rotation of the photoresponsive unit provides a high spatiotemporal resolution and control on the release profile. Our system was able to precisely turn on and off the release of calcein during sequential irradiations using light as the only stimulus over three cycles. An efficient release from the polymeric vesicles was observed after the irradiation cycles (>75% with 25 mol% of **MM2**) using low-power visible light (λ = 420 nm, 6.9 mW). Remarkably, we also demonstrate the release of a fluorescent probe when using minimal concentrations of photo-responsive units (30% release with 1 mol% of **MM2**). These results will facilitate the next applications of stimuli-responsive systems in the management of highly toxic drugs that need to be delivered with precise content control. Furthermore, our system was tested under relevant physiological conditions and successfully functioned as a drug delivery system of the chemotherapeutic agent PEM in a A549 lung carcinoma cell line. Similar levels of cell viability were observed compared to free-given drugs showing the potential of our system to deliver functional drugs on demand with the same efficiency and lower toxicity. We also proved that neither the polymer vesicles, the irradiation setup or the molecular motor content used in our experiments induced any kind of cytotoxicity to the living cells. The ability of these polymersomes containing molecular motors to release drugs on-demand using low-power visible light together with the low toxicity make our system highly relevant for further nanomedicine applications. The next steps should focus on the development and study of different release profiles by exploiting the available library of synthetic molecular motors with different rotation speeds, hydrophobicity, and chemical configurations to understand and gain further control on the release behaviour (46). Future studies should also focus on the use of longer wavelengths of light which would increase the penetration in tissue and their testing in more complex and relevant bioenvironments such as 3D cocultures of cells and in vivo setups.

To summarize, we report the first light-responsive polymersome delivery system using a synthetic rotary molecular motor as the photoresponsive unit. We validated the use of our system to controllably switch on and off the release by using low-powered visible light over sequential cycles and demonstrated the relevance by delivering a clinically approved drug used in the treatment of lung cancer cells. These results open the door to the use of synthetic molecular motors in smart delivery systems in the field of nanomedicine and bring us one step closer to the next generation of precision therapeutics.

3. Materials and Methods

3.1. Materials. Sepharose® (4B, 45 to 165 μm beads diameter), penicillin, streptomycin, PEM and Whatman® Nucleopore™ Track-Etched membranes (100 nm) were purchased from Sigma-Aldrich. PBS and fetal bovine serum (FBS) were purchased from BioConcept. Dulbecco's Modified Eagle Medium (DMEM) with GlutaMAX™ was purchased from Gibco Life Sciences. CellTiter 96® AQueous One Solution Cell Proliferation Assay (MTS) was purchased from Invitrogen. Chemicals for the synthesis of **MM2** were purchased from commercial sources; Sigma-Aldrich (DE), Fluorochem (UK), Tokyo Chemical Industry (TCI) (JP) and used without further purification. Dried solvents were obtained from Acros Organics or from a solvent purification system (MBraun SPS-800).

Irradiation experiments with λ_{max} = 420 nm were conducted using a Thorlab M429F2 model fiber-coupled LED and used at 6.9 mW.

3.2. Synthesis of Molecular Motor MM2. All compounds were synthesized according to modified literature procedures (56, 72–74). Analytical details can be found in the *SI Appendix*.

All reactions were carried out in flame-dried Schlenk tubes or oven-dried crimp top vials under a nitrogen atmosphere using standard Schlenk techniques. Solutions and reagents were added with nitrogen-flushed disposable syringes/needles. Analytical thin-layer chromatography was performed on silica gel 60 G/UV265 aluminum sheets from Merck, DE (0.25 mm). Flash column chromatography was performed on silica gel Davisil LC60A (Merck type 9385, 230 to 400 mesh) or a Reveleris X2 Flash Chromatography system from Büchi (CH) Medium-Pressure Liquid Chromatography (MPLC).

3.3. Polymersome Preparation. Synthesis and characterization of amphiphilic diblock copolymer PDMS-*block*-poly(2-methyl-2-oxazoline) ($PDMS_{25}$-*b*-$PMOXA_{10}$) was described previously (52).

Polymer vesicles were prepared by thin film hydration method followed by extrusion through polycarbonate pore membranes of desired size (100 or 200 nm) and purification by SEC. A $PDMS_{25}$-*b*-$PMOXA_{10}$ solution in EtOH (10 mg mL^{-1}) was mixed with a solution of molecular motors (1mg mL^{-1}) in EtOH or the absence of them at the desired ratio (mol% of molecular motor). The mixed solutions were vortexed and sonicated to ensure the homogeneity of the samples before the solvent was completely removed by evaporation under rotation using a stream of N_2 and 1 h vacuum. The dry films were hydrated with 1 mL PBS buffer (7.4 pH, #524650-1EA, Merck) and stirred overnight at 1,200 rpm to generate the polymersomes by self-assembly. The resulting turbid solutions were extruded 21 times using Avanti Mini Extruder (Avanti) and the corresponding polycarbonate membrane (Avanti™) prewetted in PBS buffer. Purification was performed using Sepharose™ Fast flow, 45 to 165 μm beads diameter (Amersham, UK). Sepharose™ is a spherical agarose-based SEC matrix that separates molecules by differences in size as they pass through a resin packed in a column. Molecules with partial access to the pores of the matrix are separated and elute from the column in order of decreasing size. In this way, separation of the polymer vesicles from nonincorporated MM2/Calein/PEM could be achieved (representative example in *SI Appendix*, Fig. S11). The obtained samples were used within 48 h after purification. During the experimental procedure all setups were protected from light.

3.3.1. Polymersome preparation for calcein release. For calcein release studies a similar procedure was used with the addition of a calcein solution in dimethyl sulfoxide (DMSO) (#17783, Sigma-Aldrich) was added to the PBS buffer before the thin-film hydration step to a final concentration of 0.2 mM.

3.3.2. Polymersome preparation for drug release. For drug release studies a similar procedure was used with the addition of MM2 and a PEM solution in water (Sigma-Aldrich) for the thin film hydration step to a final concentration of 0.1 mM.

3.4. Characterization of Polymersomes.

3.4.1. Light scattering. The size of the vesicles after purification was determined using a Zetasizer Ultra (MAL1255805 serial number, Malvern Panalytical, UK). Samples were measured in PBS buffer, 37 °C, seven attenuations using a disposable ZEN1002 cuvette (Malvern Panalytical) positioned at 4.64 mm from the scattering detector fixed at angle 174.7°. Irradiated samples were measured after being illuminated for 1 min with 420 nm LED (700 mA).

The shape parameter ρ (R_g/R_h) was obtained by combining dynamic and SLS measures done on a light scattering spectrometer (LS instruments), equipped with a He–Ne 21 mW laser (λ = 632.8 nm) at scattering angles from 30° to 135° at 25 °C. Guinier plots were used for obtaining the radius of gyration (R_g), while the hydrodynamic radius (R_h) was obtained from DLS.

3.4.2. Zeta-potential. Zeta-potential was measured using a Zetasizer Ultra (MAL1255805 serial number, Malvern Panalytical). Samples were diluted in water and added to a disposable folding capillary DTS1070 cuvette. The zeta-potential was recorded after each polyelectrolyte deposition (20 mV).

3.4.3. NTA. The concentration, volume, and surface area changes of the vesicles were determined using a NanoSight NS 300 instrument (NanoSight Ltd., 488 nm laser). Samples were measured in PBS buffer at room temperature.

3.4.4. UV–VIS absorption measurements. Absorption spectra of the samples were recorded on a Agilent 8453 Ultra Violet - Visible (UV–VIS) Spectroscopy System (Agilent, USA) equipped with a TC1 temperature controller (Quantum Northwest) in a 1-mm quartz cuvette, PBS buffer and 37 °C.

3.4.5. SAXS measurements. SAXS analysis was performed at the Multipurpose Instrument for Nanostructure Analysis beamline at the University of Groningen. The diffractometer was equipped with Cu rotating anode ($\lambda = 1.5413$ Å) using a sample-to-detector distance of 28.1 cm. The scattering patterns were collected using a Bruker Vantec 500 detector. The scattering angle scale was calibrated using the known position of diffraction rings from a silver behenate standard sample. The scattering intensity curves are reported as a function of the modules of the scattering vector $q = 4\pi/\lambda(\sin\theta)$, with 2θ being the scattering angle and λ the wavelength of the X-rays. The samples were placed in sealed glass capillaries and then measured under vacuum. Polymersomes samples were prepared in MilliQ with a 200 nm diameter size and a total concentration of 5 mg/mL. Samples containing **MM2** were prepared with a concentration of 25 mol% of molecular motor.

3.4.6. cryo-TEM. Polymersomes samples of 2.5 μL (2 mM) were placed on a glow-discharged holy carbon-coated grid (Quantifoil 3.5/1, QUANTIFOIL Micro Tools GmbH). After blotting, the corresponding grid was rapidly frozen in liquid ethane (Vitrobot, FEI) and kept in liquid nitrogen until measurement. The grids were observed with a Gatan model 626 cryostage in a Tecnai T20 Field Electron and Ion Company (FEI) cryo-electron microscope operating at 200 keV. Cryo-TEM images were recorded under low-dose conditions on a slow-scan Charge-Coupled Device (CCD) camera. All processes were performed in the dark. For irradiated samples, the same procedure as described before was carried out in a quartz cuvette immediately before freezing.

3.4.7. Transmission electron microscopy (TEM). Polymersomes aliquots of 5 μL (0.1 mg/mL) were adsorbed to 400 mesh square copper grids. Excess liquid was blotted and grids were negatively stained with 2% uranyl acetate. All process was performed in the dark. Micrographs of nanostructures were recorded on a Philips CM100 transmission electron microscope at an accelerating voltage of 80 kV. Irradiations were performed right before preparation of the sample.

3.5. Encapsulation/Insertion Efficiencies.

3.5.1. Estimation of molecular motor incorporation efficiency. Estimation of molecular motor encapsulation was achieved by using an absorbance standard curve of known concentration values (from 0.1 to 100 μM) of molecular motor at 405 nm. Theoretical absorbance values were calculated for each of the samples as the maximum encapsulation efficiency. Experimental absorbance values were used to estimate the amount of encapsulation for each concentration.

3.5.2. Estimation of calcein dye encapsulation efficiency. Estimation of dye encapsulation efficiency was done by taking the absorbance of a calcein 0.2 mM solution in the same sample conditions at 495 nm as the maximum value. Relative absorbance of the samples at the same wavelength was used to estimate the amount of encapsulated dye.

3.5.3. Estimation of drug encapsulation efficiency. Free drug was run through the SEC column used for the purification of polymersomes. Applying a 280 nm detector, the area under the curve of its peak was calculated employing the UNICORN software. Polymersomes containing the drug were extruded at 100 nm and purified by SEC. The amount of free drug was calculated taking the area under the curve of its peak and by subtracting it from the initial amount, the amount of encapsulated drug in the polymersomes was estimated.

3.6. Fluorescence Release Studies. Polymer vesicles containing calcein solution in PBS were used for fluorescence release studies. Fluorescent release studies were performed in a Spectrofluorometer FS5 (Edinburgh instruments) with excitation 495 nm and emission 515 nm in PBS buffer and room temperature. Fluorescence emission spectra of the calcein-loaded polymersomes with different concentrations of molecular motor was measured before and after 1 min irradiation with 420 nm light. Samples were kept in the dark for 1 h before being measured and irradiated for a maximum of three cycles. Maximum fluorescence was recorded after sonication of the samples with EtOH (1% final concentration) for 15 min. The percentage of calcein release was calculated following the equation:

$$\%\,\text{Calcein release} = 100 * \frac{(F_t - F_0)}{(F_{max} - F_0)},$$

where F_t is the fluorescence emission at the measured time, F_0 is the fluorescence emission prior to any exposure to light and F_{max} is the maximum fluorescence measured after incubation with EtOH.

3.7. Cell Culture. A549 cells (lung carcinoma, human; ATCC® CCL-185™) were routinely cultured in DMEM supplemented with 10% FBS, 100 U mL^{-1} penicillin and 100 U mL^{-1} streptomycin. Cells were maintained at 37 °C in a humidified atmosphere containing 5% CO_2.

3.7.1. Cell viability assay. Cell viability was evaluated by CellTiter 96® AQueous One solution cell proliferation assay (MTS). In brief, cells were seeded at a concentration of 3,000 cells per well in a 96-well plate (100 μL). After 24 h, 100 μL of fresh medium containing polymersomes in PBS (0.35 mg mL^{-1}) or PBS was added. The next day, the supernatant was removed, cells were rinsed once with PBS before adding fresh medium (100 μL). For irradiation at 430 nm, 96-well plates were exposed to Lite-On LEDs (six LEDs, 3.5 cm from each other, device dimensions: (13 × 9 × 3.5) cm, Mouser Electronics, 3.4 V, 50 Hz, 0.5 Ampere (AMPS), 430 nm), irradiated for 1 min and were then cultured at 37 °C for another 24 h. The supernatant was removed, and fresh medium (100 μL) was added together with MTS reagent (10 μL) to each well. After 1 h incubation at 37 °C, absorbance was measured at 490 nm using a SpectraMax plate reader. The data were normalized to PBS-treated control cells, irradiated or nonirradiated as indicated, after background absorbance removal. Statistical analysis was performed using OriginPro 2020.

For cell viability studies that did not involve polymersomes, MTS was carried out correspondingly except that after 24 h, 100 μL of fresh medium containing PEM (5 μM), supernatant of irradiated ($\lambda = 430$ nm, 1 min) polymersomes containing PEM (5 μM) or PBS was added to each well before 1 min irradiation at 430 nm.

3.8. Statistical Analysis. Pooled data is presented as mean ± SD unless otherwise indicated. Information regarding sample size, error bars and statistical analysis used is described in each figure legend. *P* values for statistical analysis of two experimental groups or for multiple comparisons were calculated using OriginLab version 2018 and 2021 (https://www.originlab.com/). Statistical significance was assessed using unpaired two-tailed *t* tests. Significance is reported following American Psychological Association (APA) guidelines (*$P \le 0.05$, **$P \le 0.01$, ***$P \le 0.001$, ****$P \le 0.0001$) (75).

Data, Materials, and Software Availability. All study data are included in the article and/or *SI Appendix*.

ACKNOWLEDGMENTS. A.G. is gratefully to Prof. Wiktor Szymanski for guidance and fruitful discussions on the project. She acknowledges Dr. Viviana Maffeis and Dr. Voichita Mihali for TEM measurements and guidance during her time in Switzerland. A.G. thanks Albert Schulte and Youxin Fu for guidance in fluorescent measurements. She gratefully thanks Dr. Romain Costil, John de Boer, Paco Visser, and Dr. George Alachouzos for fruitful discussions and support. M.K. gratefully acknowledges Dr. Cora-Ann Schoenenberger for fruitful discussions and guidance for the cell experiments. Financial support was granted from BIOMOLMACS, a European project funded by the European Union's Horizon 2020 research and innovation program under the Marie Skłodowska-Curie grant agreement no. 859416 to A.G. and M.K. and the European Research Council (Advanced Investigator Grant no. 694345 to B.L.F.). M.K., I.A.D. and C.P. acknowledge the University of Basel, and I.A.D. and C.P. thank the National Centre of Competence in Research–Molecular Systems Engineering for their financial support. We take the opportunity to thank the late Prof. Dr. Wolfgang P. Meier for his support and supervision of the project until he passed away in January 2022.

Author affiliations: [a]Faculty of Science and Engineering, Stratingh Institute for Chemistry, University of Groningen, 9747 AG Groningen, The Netherlands; [b]Department of Chemistry, University of Basel, BPR 1096, 4058 Basel, Switzerland; [c]Faculty of Science and Engineering, Zernike Institute for Advanced Materials, University of Groningen, 9747 AG Groningen, The Netherlands; [d]National Centre of Competence in Research-Molecular Systems Engineering, BioPark Rosental 1095 Basel, Switzerland; and [e]Swiss Nanoscience Institute, University of Basel, 4056 Basel, Switzerland

1. K. Kostarelos, The emergence of nanomedicine: A field in the making. *Nanomedicine* **1**, 1–3 (2006).
2. R. Jia *et al.*, Advances in multiple stimuli-responsive drug-delivery systems for cancer therapy. *Int. J. Nanomed.* **16**, 1525–1551 (2021).
3. S. N. Bhatia, X. Chen, M. A. Dobrovolskaia, T. Lammers, Cancer nanomedicine. *Nat. Rev. Cancer* **22**, 550–556 (2022).
4. M. S. Sudheesh, K. Pavithran, S. M, Revisiting the outstanding questions in cancer nanomedicine with a future outlook. *Nanoscale Adv.* **4**, 634–653 (2022).
5. H. Jahangirian, E. G. Lemraski, T. J. Webster, R. Rafiee-Moghaddam, Y. Abdollahi, A review of drug delivery systems based on nanotechnology and green chemistry: Green nanomedicine. *Int. J. Nanomed.* **12**, 2957–2978 (2017).
6. M. J. Mitchell *et al.*, Engineering precision nanoparticles for drug delivery. *Nat. Rev. Drug Discov.* **20**, 101–124 (2021).
7. J. K. Patra *et al.*, Nano based drug delivery systems: Recent developments and future prospects. *J. Nanobiotechnol.* **16**, 1–33 (2018).
8. S. S. Suri, H. Fenniri, B. Singh, Nanotechnology-based drug delivery systems. *J. Occup. Med. Toxicol.* **2**, 1–6 (2007).
9. A. Z. Wilczewska, K. Niemirowicz, K. H. Markiewicz, H. Car, Nanoparticles as drug delivery systems. *Pharmacol. Rep.* **64**, 1020–1037 (2012).
10. A. D. Bangham, R. W. Horne, Negative staining of phospholipids and their structural modification by surface-active agents as observed in the electron microscope. *J. Mol. Biol.* **8**, 660–668 (1964).
11. M. R. Shah, M. Imran, S. Ullah "Chapter 3 - liposomes" in *Lipid-Based Nanocarriers for Drug Delivery and Diagnosis*, M. R. Shah, M. Imran, S. Ullah, Eds. (Micro and Nano Technologies, William Andrew Publishing, 2017), pp. 63–110.
12. T. Date *et al.*, Lipid-polymer hybrid nanocarriers for delivering cancer therapeutics. *JCR* **271**, 60–73 (2018).
13. S. H. Kiaie *et al.*, Axial pharmaceutical properties of liposome in cancer therapy: Recent advances and perspectives. *Int. J. Pharm.* **581**, 119269 (2020).
14. Y. Barenholz, Doxil® - The first FDA-approved nano-drug: Lessons learned. *JCR* **160**, 117–134 (2012).
15. D. D. Lasic, P. M. Frederik, M. C. A. Stuart, Y. Barenholz, T. J. McIntosh, Gelation of liposome interior A novel method for drug encapsulation. *FEBS Lett.* **312**, 255–258 (1992).
16. L. Sercombe *et al.*, Advances and challenges of liposome assisted drug delivery. *Front. Pharmacol.* **6**, 1–13 (2015).
17. S. A. Moosavian, V. Bianconi, M. Pirro, A. Sahebkar, Challenges and pitfalls in the development of liposomal delivery systems for cancer therapy. *Semin. Cancer Biol.* **69**, 337–348 (2021).
18. D. Pentak, A. Ploch-Jankowska, A. Zięba, V. Kozik, The advances and challenges of liposome-assisted drug release in the presence of serum albumin molecules: The influence of surrounding pH. *Materials* **15**, 1586 (2022).
19. E. Rideau, R. Dimova, P. Schwille, F. R. Wurm, K. Landfester, Liposomes and polymersomes: A comparative review towards cell mimicking. *Chem. Soc. Rev.* **47**, 8572–8610 (2018).
20. Y. Kiel Sung, S. Wan Kim, Recent advances in polymeric drug delivery carrier systems. *Biomater. Res.* **24**, 12 (2020).
21. L. Zartner, V. Maffeis, C.-A. Schoenenberger, I. A. Dinu, C. G. Palivan, Membrane protein channels equipped with a cleavable linker for inducing catalysis inside nanocompartments. *J. Mater. Chem. B* **9**, 9012–9022 (2021).
22. A. Hafner, J. Lovrić, G. P. Lakoš, I. Pepić, Nanotherapeutics in the EU: An overview on current state and future directions. *Int. J. Nanomed.* **9**, 1005–1023 (2014).
23. S. Hossen *et al.*, Smart nanocarrier-based drug delivery systems for cancer therapy and toxicity studies: A review. *J. Adv. Res* **15**, 1–18 (2019).
24. E. Askari *et al.*, Stimuli-responsive hydrogels for local post-surgical drug delivery. *Gels* **6**, 14 (2020).
25. Q. Tang *et al.*, Stimuli responsive nanoparticles for controlled anti-cancer drug release. *Curr. Med. Chem.* **25**, 1837–1866 (2018).
26. Y. Mu, L. Gong, T. Peng, J. Yao, Z. Lin, Advances in pH-responsive drug delivery systems. *OpenNano* **5**, 100031 (2021).
27. D. Ghosh Dastidar, G. Chakrabarti, "Chapter 6 - thermoresponsive drug delivery systems, characterization and application" in *Applications of Targeted Nano Drugs and Delivery Systems*, S. S. Mohapatra, S. Ranjan, N. Dasgupta, R. K. Mishra, S. Thomas, Eds. (Micro and Nano Technologies, Elsevier, 2019), pp. 133–155.
28. H. Y. Yang, Y. Li, D. S. Lee, Multifunctional and stimuli-responsive magnetic nanoparticle-based delivery systems for biomedical applications. *Adv. Ther. (Weinh)* **1**, 1800011 (2018).
29. B. Qian, Q. Zhao, X. Ye, Ultrasound and magnetic responsive drug delivery systems for cardiovascular application. *J. Cardiovasc. Pharmacol.* **76**, 414–426 (2020).
30. Y. Liu *et al.*, An electric-field responsive microsystem for controllable miniaturised drug delivery applications. *Procedia Eng.* **25**, 984–987 (2011).
31. M. Li, G. Zhao, W. K. Su, Q. Shuai, Enzyme-responsive nanoparticles for anti-tumor drug delivery. *Front. Chem.* **8**, 1–20 (2020).
32. P. V. Torchin *et al.*, *Stimuli-responsive Drug Delivery Systems*, A. Singh, M. M. Amiji, Eds. (Royal Society of Chemistry, 2018).
33. S. H. Yun, S. J. J. Kwok, Light in diagnosis, therapy and surgery. *Nat. Biomed. Eng.* **1**, 0008 (2017).
34. Z. L. Pianowski, B. L. Feringa, *Molecular Photoswitches: Chemistry, Properties, and Applications, 2 Volume Set* (2022), 10.1002/9783527827626.
35. Y. Yao *et al.*, Azobenzene-based cross-linked small-molecule vesicles for precise oxidative damage treatments featuring controlled and prompt molecular release. *Chem. Mater.* **33**, 7357–7366 (2021).
36. A. Koçer, M. Walko, W. Meijberg, B. L. Feringa, Chemistry: A light-actuated nanovalve derived from a channel protein. *Science* **1979**, 755–758 (2005).
37. B. M. Vickerman, E. M. Zywot, T. K. Tarrant, D. S. Lawrence, Taking phototherapeutics from concept to clinical launch. *Nat. Rev. Chem.* **5**, 816–834 (2021).
38. Y. Matsumura, H. N. Ananthaswamy, Toxic effects of ultraviolet radiation on the skin. *Toxicol. Appl. Pharmacol.* **195**, 298–308 (2004).
39. I. M. Welleman, M. W. H. Hoorens, B. L. Feringa, H. H. Boersma, W. Szymański, Photoresponsive molecular tools for emerging applications of light in medicine. *Chem. Sci.* **11**, 11672–11691 (2020).
40. D. Mulatihan, T. Guo, Y. Zhao, Azobenzene photoswitch for isomerization-dependent cancer therapy via azo-combretastatin A4 and phototrexate. *Photochem. Photobiol.* **96**, 1163–1168 (2020).
41. G. Wang, J. Zhang, Photoresponsive molecular switches for biotechnology. *J. Photochem. Photobiol. C* **13**, 299–309 (2012).
42. A. Galvan-Gonzalez *et al.*, Photodegradation of azobenzene nonlinear optical chromophores: The influence of structure and environment. *JOSA B.* **17**, 1992 (2000).
43. J. M. Joseph, H. Destaillats, H. M. Hung, M. R. Hoffmann, The sonochemical degradation of azobenzene and related azo dyes: Rate enhancements via fenton's reactions. *J. Phys. Chem* **104**, 301–307 (2000).
44. Technical Report Series (No. 154), Bioassay of azobenzene for possible carcinogenicity. National Cancer Institute (1979).
45. J. C. M. Kistemaker, A. S. Lubbe, B. L. Feringa, Exploring molecular motors. *Mater. Chem. Front.* **5**, 2900–2906 (2021).
46. D. R. S. Pooler, A. S. Lubbe, S. Crespi, B. L. Feringa, Designing light-driven rotary molecular motors. *Chem. Sci.* **12**, 14964–14986 (2021).
47. N. Koumura, R. W. J. Zijlstra, R. A. van Delden, N. Harada, B. L. Feringa, Light-driven monodirectional molecular rotor. *Nature* **401**, 152–154 (1999).
48. C. Stähler *et al.*, Light-driven molecular motors embedded in covalent organic frameworks. *Chem. Sci.* **13**, 8253–8264 (2022).
49. T. Freese *et al.*, A molecular motor from lignocellulose. *Green Chem.* **24**, 3689–3696 (2022).
50. F. Xu *et al.*, Dynamic control of a multistate chiral supramolecular polymer in water. *JACS* **144**, 6019–6027 (2022).
51. S. Chen *et al.*, Photoactuating artificial muscles of motor amphiphiles as an extracellular matrix mimetic scaffold for mesenchymal stem cells. *JACS* **144**, 3543–3553 (2022).
52. C. E. Meyer, I. Craciun, C.-A. Schoenenberger, R. Wehr, C. G. Palivan, Catalytic polymersomes to produce strong and long-lasting bioluminescence. *Nanoscale* **13**, 66–70 (2021).
53. C. G. Palivan *et al.*, Bioinspired polymer vesicles and membranes for biological and medical applications. *Chem. Soc. Rev.* **45**, 377–411 (2016).
54. E. Brodszkij *et al.*, Polymer-lipid hybrid vesicles and their interaction with HepG2 Cells. *Small* **16**, 1–9 (2020).
55. M. Korpidou *et al.*, Inverting glucuronidation of hymecromone in situ by catalytic nanocompartments. *J. Mater. Chem. B.* **10**, 3916–3926 (2022).
56. J. Chen, K. Y. Chen, G. T. Carroll, B. L. Feringa, Facile assembly of light-driven molecular motors onto a solid surface. *Chem. Comm.* **50**, 12641–12644 (2014).
57. M. Hernandes, S. M. Cavalcanti, D. R. Moreira, W. de Azevedo Jr., A. C. Leite, Halogen atoms in the modern medicinal chemistry: Hints for the drug design. *Curr. Drug Targets* **11**, 303–314 (2010).
58. V. García-López *et al.*, Molecular machines open cell membranes. *Nature* **548**, 567–572 (2017).
59. G. Pabst, M. Rappolt, H. Amenitsch, P. Laggner, Structural information from multilamellar liposomes at full hydration: Full q-range fitting with high quality X-ray data. *Phys. Rev. E Stat. Phys. Plasmas Fluids Relat. Interdiscip. Topics* **62**, 4000–4009 (2000).
60. G. N. I. Clark, G. L. Hura, J. Teixeira, A. K. Soper, T. Head-Gordon, Small-angle scattering and the structure of ambient liquid water. *Proc. Natl. Acad. Sci. U.S.A.* **107**, 14003–14007 (2010).
61. L. K. E. A. Abdelmohsen, R. S. M. Rikken, P. C. M. Christianen, J. C. M. van Hest, D. A. Wilson, Shape characterization of polymersome morphologies via light scattering techniques. *Polymer (Guildf)* **107**, 445–449 (2016).
62. T. L. Doane, C.-H. Chuang, R. J. Hill, C. Burda, Nanoparticle ζ -Potentials. *Acc. Chem. Res.* **45**, 317–326 (2012).
63. D. F. Swinehart, The Beer-Lambert law. *J. Chem. Educ.* **39**, 333 (1962).
64. C. E. Meyer, C.-A. Schoenenberger, R. P. Wehr, D. Wu, C. G. Palivan, Artificial melanogenesis by confining melanin/polydopamine production inside polymersomes. *Macromol. Biosci.* **21**, 2100249 (2021).
65. S. Hamann *et al.*, Measurement of cell volume changes by fluorescence self-quenching. *J. Fluoresc.* **12**, 139–145 (2002).
66. S. Chattopadhyay, R. G. Moran, I. D. Goldman, Pemetrexed: Biochemical and cellular pharmacology, mechanisms, and clinical applications. *Mol. Cancer Ther.* **6**, 404–417 (2007).
67. K. Soni, A. Mujtaba, K. Kohli, Lipid drug conjugate nanoparticle as a potential nanocarrier for the oral delivery of pemetrexed diacid: Formulation design, characterization, ex vivo, and in vivo assessment. *Int. J. Biol. Macromol.* **103**, 139–151 (2017).
68. R. Pangeni, J. U. Choi, V. K. Panth, Y. Byun, J. W. Park, Enhanced oral absorption of pemetrexed by ion-pairing complex formation with deoxycholic acid derivative and multiple nanoemulsion formulations: Preparation, characterization, and in vivo oral bioavailability and anticancer effect. *Int. J. Nanomed.* **13**, 3329–3351 (2018).
69. R. Maharjan *et al.*, Metronomic delivery of orally available pemetrexed-incorporated colloidal dispersions for boosting tumor-specific immunity. *Drug Delivery* **28**, 2313–2328 (2021).
70. V. Balasubramanian *et al.*, A surprising system: Polymeric nanoreactors containing a mimic with dual-enzyme activity. *Soft Matter* **7**, 5595–5603 (2011).
71. A. A. Adjei, Pharmacology and mechanism of action of pemetrexed. *Clin. Lung Cancer* **5**, S51–S55 (2004).
72. B. Kobin, L. Grubert, S. Blumstengel, F. Henneberger, S. Hecht, Vacuum-processable ladder-type oligophenylenes for organic-inorganic hybrid structures: Synthesis, optical and electrochemical properties upon increasing planarization as well as thin film growth. *J. Mater. Chem.* **22**, 4383–4390 (2012).
73. U. Dietrich, M. Hackmann, B. Rieger, M. Klinga, M. Leskelä, Control of stereoerror formation with high-activity "dual-side" zirconocene catalysts: A novel strategy to design the properties of thermoplastic elastic polypropenes. *JACS* **121**, 4348–4355 (1999).
74. W. Danowski *et al.*, Unidirectional rotary motion in a metal–organic framework. *Nat. Nanotechnol.* **14**, 488–494 (2019).
75. American Psychological Association, "APA style numbers and statistics guide" in *APA Publication Manual Sections 6.32-6.35*, (2022), p. 2.